On the formation mechanisms of artificially generated high Reynolds number turbulent boundary layers

Eduardo Rodríguez-López · Paul J.K. Bruce · Oliver R.H. Buxton

Abstract We investigate the evolution of an artificially thick turbulent boundary layer generated by two families of small obstacles (divided into uniform and non-uniform wall normal distributions of blockage). One- and two-point velocity measurements using constant temperature anemometry show that the canonical behaviour of a boundary layer is recovered after an adaptation region downstream of the trips presenting 150% higher momentum thickness (or equivalently, Reynolds number) than the natural case for the same downstream distance ($x \approx 3\,\mathrm{m}$). The effect of the degree of immersion of the obstacles for $h/\delta \gtrsim 1$ is shown to play a secondary role. The one-point diagnostic quantities used to assess the degree of recovery of the canonical properties are the friction coefficient (representative of the inner motions), the shape factor and wake parameter (representative of the wake regions); they provide a severe test to be applied to artificially generated boundary layers. Simultaneous two-point velocity measurements of both spanwise and wall-normal correlations and the modulation of inner velocity by the outer structures show that there are two different formation mechanisms for the boundary layer. The trips with high aspect ratio and uniform distributed blockage leave the inner motions of the boundary layer relatively undisturbed, which subsequently drive the mixing of the obstacles' wake with the wall-bounded flow (wall-driven). In contrast, the low aspect-ratio trips with non-uniform blockage destroy the inner structures, which are then re-formed further downstream under the influence of the wake of the obstacles (wake-driven).

1 Introduction

Obtaining a high Reynolds number (Re) in wall-bounded flow is of primary importance from two perspectives. First, in order to study the asymptotic values of different properties of the flow, and secondly, for relevant engineering applications such as pollutant dispersion or loads over buildings immersed in the atmospheric boundary layer. This necessity for highly reliable high Re experiments and simulations in wall-bounded flows has been assessed in the last few years, e.g. Marusic et al (2010) or Klewicki (2010) amongst others. Given that, for existing computational facilities, the achievable Re in direct numerical simulation is lower than in experiments, several research groups have the objective of obtaining and studying high fidelity high Re experiments. Some examples of these facilities are: the Princeton Superpipe (McKeon et al 2003), the national diagnosis facility (NDF) in Illinois (Vinuesa 2013), the minimum turbulence level (MTL) wind tunnel in Stockholm (Österlund 1999) or the high Reynolds number boundary layer wind tunnel (HRNBLWT) in Melbourne (Nickels et al 2007). Other studies use the stable flow conditions present in the atmospheric boundary layer such as, for instance, the salt playa in the Utah dessert (Metzger and Klewicki 2001) or seek the building of new facilities (Talamelli et al 2009) or sensors (Bailey et al 2010).

Eduardo Rodríguez-López
Imperial College London Exhibition Road, London, United Kingdom
Tel.: +44-(0)20-75941976
E-mail: eduardo.rodriguez-lopez12@imperial.ac.uk

Paul J.K. Bruce
Imperial College London

Oliver R.H. Buxton
Imperial College London

Further, from a purely scientific and fundamental point of view, obtaining a high Re turbulent boundary layer (TBL) is also a constraint for some wind-tunnel flows. Briefly, for testing elements that are immersed in a boundary layer (such as pollutant dispersion or civil structures in an atmospheric boundary layer) the ratio between the characteristic length of the model and the boundary layer should be kept as close as possible to reality. This requires obtaining an extremely thick TBL, which, for a given freestream velocity, is equivalent to artificially increasing the Reynolds number. This problem has been solved in many ways during the past decades, among them it is worth mentioning the work of Armitt and Counihan (1968); Counihan (1969) who used spires for the first time in the shape of a quarter of ellipsoid combined with roughness elements in order to increase the TBL thickness in the test section downstream of the obstacles. This method has been broadly used and improved, e.g. Arie et al (1981) or Davidson et al (1996) amongst many others. Other devices have also been used in the past to artificially thicken the boundary layer such as a non-uniform blockage grid (Kornilov and Boiko 2013), fences and jets normal to the flow (Sargison et al 2004), a jet opposed to the flow (Nagib et al 1976), small cylinders normal to the wall (Kornilov and Boiko 2012) or a combination of several of those methods (Cook 1978). A review of other techniques can be found for instance in Hunt and Fernholz (1975).

The main similarities between these methods are the quality tests that are employed in order to verify whether the obtained artificially thick TBL achieves the desired state. Usually these conditions are mainly based on the mean profile, turbulence intensity and integral scale distributions; it is sufficient to validate those criteria for most engineering applications. However, there is a considerable gap between the properties of the TBL obtained by any of these means and the current requirements of canonical high Re experiments such as those summarized above. With the arguable exception of Kornilov and Boiko (2012), who based part of their conclusions on the Clauser equilibrium parameter, the present paper is among the first aiming to link both strategies; namely, the ability to generate an artificially thick TBL but ensuring that its properties resemble the high Reynolds number studies mentioned in the first paragraph. In summary, whilst the aim is to generate an artificially thick (high Re) boundary layer, the criteria used to assess its properties will be considerably more demanding than those that appear usually in the frame of atmospheric boundary layer simulations.

In particular, results are presented using one- and two-point velocity statistics studying the downstream evolution of a turbulent boundary layer disturbed with relatively small obstacles. Measurements are presented concerning one- and two-point streamwise velocity fluctuations (no results of the wall-normal and spanwise velocity components are presented). Note that two-point statistics are essential to understanding the underlying eddy structure in the boundary layer and they are necessary in order to explain some of the features of single-point measurements (Hutchins and Marusic 2007b; Mathis et al 2009). From a slightly different perspective, the eddy structure of the flow is responsible for the Reynolds stresses (such as $u'v'$ events); hence the study of two-points statistics represents a more demanding test to ensure that the turbulent structure of the flow is recovered. These measurements also play a crucial role in studying the formation mechanisms downstream of various obstacles as a function of the trip particular geometry, which is one of the main scopes of the present study.

The objective of the trips is to generate both a velocity defect and a high turbulence intensity level in such a way that the TBL grows more rapidly. This study will only consider two families of small obstacles and pay attention to the ensuing adaptation region. First, one can consider a uniform distribution of low blockage in the wall-normal direction in order to generate a uniform forcing in the wall-normal direction, y. This constant blockage would generate a spanwise combination of wakes and jets without a drastic modification of the inner structures of the boundary layer (Kornilov and Boiko 2012). Second, introducing a non-uniform blockage in y varying from 100% for $y = 0$ to zero at the height of the trips would destroy completely the incoming inner structures forcing them to re-form at some point downstream of the trips (Sargison et al 2004). These trips with non-uniform blockage create a distorted wake which, after an adaptation region, may influence the formation of the inner structures up to a larger extent than in the former case, where the inner structures may not be as disturbed due to the low blockage at $y = 0$. This influence of the wake in the near-wall region has also been reported as a characteristic of re-attached flows downstream of a separation (Alving and Fernholz 1996; Castro and Epik 1998). Different heights and degrees of immersion in the boundary layer are tested in order to assess the influence of these parameters on the recovery length for canonical properties of the generated boundary layer.

Regarding the one-point measurements the main criteria are those proposed by Chauhan et al (2009); note that these criteria have been considered recently to assess the validity of naturally growing TBLs, thus applying them to an artificially thick TBL constitutes a more demanding test given the sensitivity of this criterion to initial and boundary conditions. Furthermore, in the last decade special attention has been paid to the measurement of the interaction between inner and outer structures by their degree of

modulation (Mathis et al 2009). These effects, together with the eddy structure can only be measured by two-point statistics, both in the spanwise and wall-normal directions. Thus, studies will be presented in this paper in order to ensure that the artificially high Re TBL created presents not only canonical properties for one-point measurements, but also reproduces the eddy structure of the undistorted case. Two-point statistics also present a high relevance in order to discern the distinct formation mechanisms present downstream of the different families of obstacles.

Summarizing, the present study attempts to link together the two mentioned approaches. It shows how to use techniques for the artificial generation of thick turbulent boundary layers combined with an accurate and highly demanding canonical description of the properties of a high Re TBL. We show that it is possible to generate an artificially thick TBL that resembles to the maximum accuracy the canonical properties of a high Re flow. Moreover, we assess the distinct mechanisms of formation for various families of trips depending on their wall-normal distribution of the blockage ratio.

The structure of the paper is as follows: Sect. 2 provides a description of the experimental methods used and the different configurations of obstacles chosen. Section 3 presents the results of single-point measurements and gives a possible explanation for the distinct behaviour based on the formation mechanisms within each TBL. Section 4 shows the two-point measurements presenting results about eddy structure and outer-inner interactions aiming to verify the previous hypothesis. Finally Sect. 5 draws conclusions.

2 Experimental methodology

Experiments were conducted at Imperial College London in a wind tunnel of $0.91 \times 0.91 \, \text{m}^2$ section and $4.8 \, \text{m}$ length and freestream velocity, $u_e = 10 \, \text{m s}^{-1}$. In these conditions, the incoming freestream turbulence level is $\lesssim 0.05\%$; the same wind tunnel has been broadly documented before e.g. Mazellier and Vassilicos (2010) or Valente and Vassilicos (2014).

A wooden flat plate is mounted vertically spanning the whole wind tunnel, and an elliptic (10 : 1) leading edge is mounted to avoid any separation and a trailing edge flap in order to modify the position of the stagnation point in the leading edge. A strip of sand paper $20 \, \text{mm}$ long, is placed at $x = 100 \, \text{mm}$ (right after the elliptic leading edge) to ensure the transition into a TBL. Due to experimental limitations, velocity measurements can only be taken in the central $3 \, \text{m}$ of the test section. Therefore, two different configurations ($P1$ and $P2$) of the flat plate are used, in order to allow measurements close to the leading edge and the trips ($P1$) and further downstream ($P2$). A sketch of the two configurations of the plate inside the wind tunnel is shown in Fig. 1. Note that, although the distance from the leading edge to the beginning of the test section varied from $0.8 \, \text{m}$ to $0 \, \text{m}$ for configurations $P1$ and $P2$ respectively, the flow conditions remained virtually constant and any minor variations are not expected to play any role in the study. The pressure gradient for both configurations is measured and shown in Fig. 2; the strongly positive pressure gradient present in the last part of the plate for both configurations is due to the presence of the flap. The location of the velocity measurements is chosen such that it is not influenced by this effect. Except where otherwise stated the coordinate system defines x as the streamwise distance downstream of the plate leading edge, y as the wall-normal distance from the plate, and z as the spanwise distance relative to the centreline. The superscript + is used for magnitudes expressed in wall units, i.e. non-dimensionalized with the viscosity, ν, and the friction velocity, $u_\tau = \sqrt{\tau_{wall}/\rho}$ where τ_{wall} is the wall-shear stress and ρ is the air density. In particular a wall unit is defined as $\delta_\nu = \nu/u_\tau$, thus $y^+ = y/\delta_\nu$, $u^+ = u/u_\tau$ and $t^+ = tu_\tau^2/\nu$.
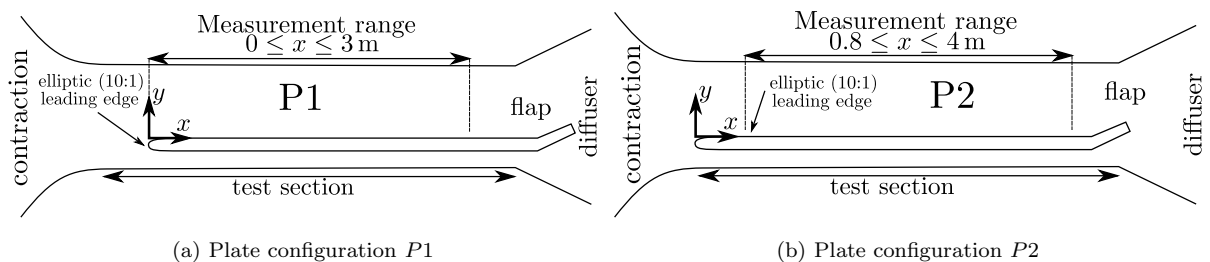

(a) Plate configuration $P1$ (b) Plate configuration $P2$

Fig. 1: Top view of plate configurations $P1$ and $P2$ in the wind tunnel.

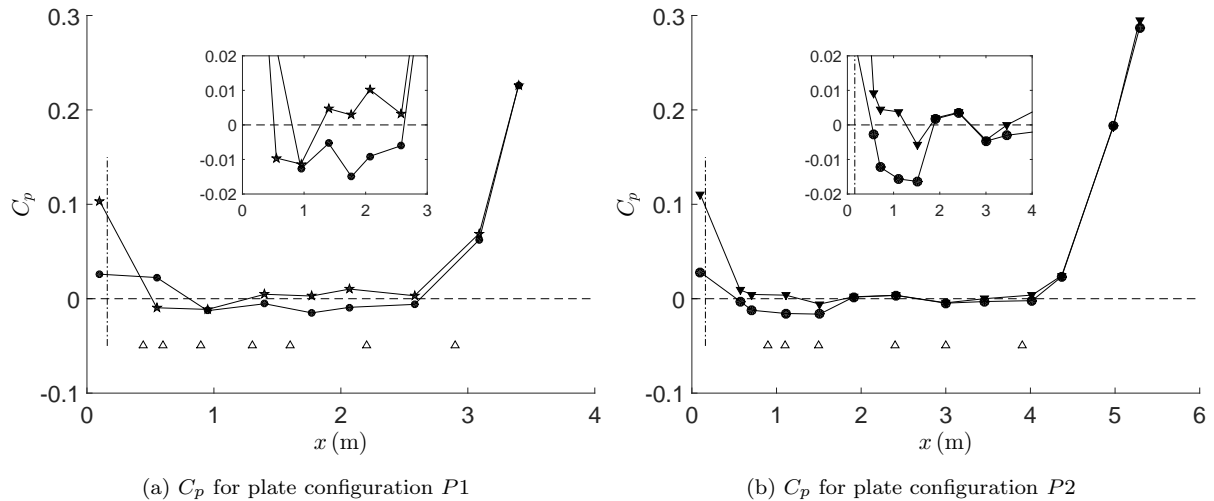(a) C_p for plate configuration $P1$ (b) C_p for plate configuration $P2$

Fig. 2: Pressure distribution for natural ($\bullet$) and tripped ($\star, \triangledown$) cases. Symbols are given in Table 1, $C_p = \frac{p - p_{ref}}{\frac{1}{2}\rho u_e^2}$, and locations of velocity measurements ($\triangle$) for both plate configurations. Dot-dashed line marks the location of the trips, $x_t = 160\,\mathrm{mm}$.

2.1 One-point velocity measurements

Measurements were taken using hot-wire anemometry. The body of a Dantec Dynamics 55P05 hot-wire probe is etched in-house using a $d_w = 5\,\mu\mathrm{m}$ Wollaston wire with a sensing length $l_w \approx 1\,\mathrm{mm}$ in order to ensure $l_w/d_w \geq 200$ as suggested by Comte-bellot (1976) or Hutchins et al (2009) amongst others. Voltage signals are recorded using a Dantec Streamline in constant temperature mode. The frequency response of the wire is checked by means of a square wave test providing a frequency response of at least $30\,\mathrm{kHz}$. Sampling at $100\,\mathrm{kHz}$ for $30\,\mathrm{s}$ and low-pass filtering at $30\,\mathrm{kHz}$ (in order to avoid aliasing) allows a resolution of $0.2 < t^+ < 0.5$ for the different downstream positions. The hot-wire was calibrated against a straight Pitot tube located parallel to the incoming flow and the temperature was monitored to ensure that it varied $< 0.5\,\mathrm{K}$ during the test and between the test calibration.

One-point measurements were taken with the flat plate set-up in the $P1$ configuration and velocity profiles were acquired at the seven downstream locations shown in Fig. 2a. The accurate wall-probe relative position as well as the friction velocity, u_τ, were extrapolated from the velocity profile using the method described in Rodríguez-López et al (2015a). Briefly, this method compares the experimentally measured velocity profile with a canonical description of the boundary-layer without any previous hypothesis on the conditions of the flow; it only requires the existence of the logarithmic layer and an empirical dependence between the two parameters of the logarithmic law. In particular the von Kármán constant, κ, is left free to adopt the value that best fits the measured flow. The accuracies on the determination of the friction velocity and the wall-probe location are $\Delta u_\tau < 1\%$ and $\Delta y^+ < 0.5$ respectively.

2.2 Two-point velocity measurements

In order to perform two-point simultaneous velocity measurements a new device with a hot-wire embedded within the wall with the prongs normal to the plate was used. The support of the wall hot-wire is mounted behind the plate attached to a linear traverse system (Fig. 3b) and it is able to position the sensor in the range $y \leq 3.5\,\mathrm{mm}$ with a resolution of $10\,\mu\mathrm{m}$. In order to know the accurate wall-probe location, a small velocity profile is taken for $y < 3\,\mathrm{mm}$ and then the accurate wall-probe relative position is extrapolated together with the wall shear stress by comparison with the canonical velocity profile of the inner layer. The post-processing method is described in Rodríguez-López et al (2015a). It has to be slightly modified to take into consideration only the points located within the inner and logarithmic regions ($6 \lesssim y^+ \lesssim 100$) in contrast with the general method where the whole velocity profile ($0 \lesssim y^+ \lesssim \delta^+$) is fitted to the experimental method.

Regarding the sensing part of the wall hot-wire, it is made from a 55P01 Dantec Dynamics probe in-house etched with a Wollaston wire of $d_w = 2.5\,\mu\mathrm{m}$ and $l_w \approx 0.5\,\mathrm{mm}$. Due to the extreme fragility of the sensor it had to be soldered to the tip of the prongs and etched *in situ*. Therefore the hot-wire

had to be calibrated while mounted in the insert. In order to do so, the second hot-wire is located at the same $\{x, y\}$ position but with a slight offset in z, enough to avoid prong interference (Fig. 3c), then the wall hot-wire was calibrated against the free hot-wire. In this case the free hot-wire was made from the body of a 55P05 Dantec Dynamics hot-wire in house etched with a Wollaston wire of $d_w = 2.5\,\mu$m and $l_w \approx 0.5$ mm. During the acquisition, both hot-wires were simultaneously sampled at 100 kHz for 40 s and low-pass filtered at 30 kHz to avoid aliasing.

(a) Frontal view in wall-normal config-uration

(b) Side view and traverse system

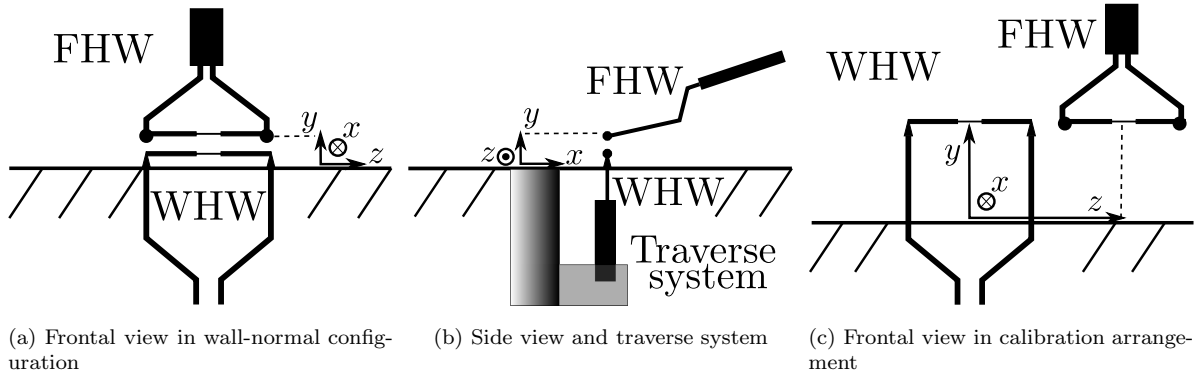(c) Frontal view in calibration arrange-ment

Fig. 3: Sketches of the wall mounted hot-wire (WHW) and the free hot-wire (FHW) in different config-urations.

Two-point measurements were taken using only the $P2$ configuration and taking three different veloc-ity profiles for each of the x locations shown in Fig. 2b. These velocity profiles were two sets of spanwise two-point measurements (Fig. 3c) and one set of wall-normal two-point velocity measurements (Fig. 3a). In the spanwise profiles the free hot-wire was set at the same $\{x, y\}$ position of the wall hot-wire (fixed) and then moved along the z direction. For the wall-normal velocity profiles the free hot-wire was set at the same $\{x, z\}$ position of the wall hot-wire and, starting as close as possible in the y direction, was traversed out from the wall. This minimum separation was found to be $\Delta y_0 \approx 0.5$ mm corresponding to $\Delta y_0^+ > 13$. The typical height of the wall hot-wire was set to be $y \approx 0.25$ mm corresponding to $6 \leq y^+ \leq 9$ for the different cases. This location was chosen as representative of inner motions of the boundary-layer but out of the viscous sublayer where the viscosity plays a major role. The accurate relative position between the two hot-wires cannot be extrapolated from the velocity profile (Rodríguez-López et al 2015a) and was instead measured by means of a digital microscope in the vicinity of both probes. The friction velocity was determined from the mean velocity profile acquired with the free hot-wire as described in Sect. 2.1.

2.3 Description of the trips

Various trips were employed in order to generate the aforementioned different effects in the evolution of the flow. To obtain a uniform wall-normal blockage distribution different arrays of spanwise distributed cylinders were used, in particular one or two rows of cylinders of different heights following Kornilov and Boiko (2012). The family of trips with a non-uniform distribution of blockage in the wall-normal direction is obtained by means of a sawtooth serrated fence following Sargison et al (2004). The exact details of the geometry of the various trips as well as the names used to refer to them are summarized in Table 1. When the obstacle is formed by two rows of cylinders the second row is always located downstream of the first one except in the *2stag20* case where the second row of cylinders is staggered and located downstream of the gaps of the first row.

In order to simulate the influence of different degrees of immersion in the boundary-layer the trips were the same in every case but they were located at different downstream locations. The two positions of the trips in the flat plate were $x_t = 160$ mm and $x_t = 890$ mm where $Re_\tau = \delta u_\tau/\nu = \{98, 556\}$, $\theta = \{0.35, 1.78\}$ mm and $\delta_\gamma = \{3.5, 19.9\}$ mm respectively. These positions correspond to two levels of immersion: $h/\delta_\gamma \gg 1$ and $h/\delta_\gamma \lesssim 1$, noting that δ_γ is defined as the first point measured without turbulent intermittency, γ, as defined by Klebanoff (1954). The selection of this, perhaps less conventional, definition of the boundary-layer thickness is justified by the structure of the boundary-layer. Although one can define, for instance, δ_{99} as the limit of the TBL, the structure of the turbulence in the wake regions
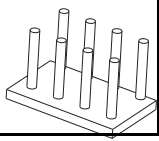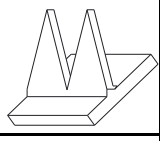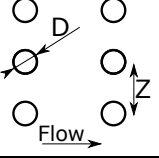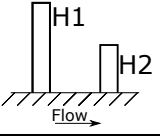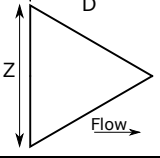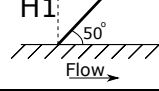
	1row10	1row20	2row10	10and20	20and10	2row20	2stag20	Saw Inv	Saw	Natural	Cyl	Saw
Type				Cyl					Saw	—		
Symbol	△	∗	▷	+	◇	⋆	□	◁	▽	○		
H1(mm)	10	20	10	10	20	20	20	15.3	15.3	0		
H2(mm)	0	0	10	20	10	20	20	-	-	0		
D(mm)	3	3	3	3	3	3	3	-12.8	12.8	0		

Table 1: Trips description. $Z = 10\,\text{mm}$ for Cyl and $Z = 20\,\text{mm}$ for Saw. $h = max\{H1, H2\}$. Three dimensional sketches are shown in the last two columns for each family of trips. Last row shows top and lateral views for the *Cyl* family (left) and *Saw* family (right)

presents a high intermittency with bulges of turbulent fluid passing followed by zones of irrotational flow. We can observe for instance in Klebanoff (1954) that for $0.5 \lesssim y/\delta_{99} \lesssim 1.3$ the intermittency factor defined as

$$\gamma(y) = \frac{3\left(\overline{u'^2}\right)^2}{\overline{u'^4}} \tag{1}$$

is $0 \leq \gamma \leq 1$, meaning that patches of rotational and irrotational flow can appear at a certain y for different times. Since the qualitative flow structure is not changing for $0.5 \lesssim y/\delta_{99} \lesssim 1.3$, choosing δ_γ can be seen as the last point where this intermittent behaviour occurs thus having the trips fully immersed in the surrounding turbulent flow. In practice δ_γ is defined as the height over the wall where the intermittency falls below a threshold level $2\gamma_{freestream}$. Note also that this definition is almost equivalent to the thickness of the boundary-layer obtained from the fitting of the velocity profile ($\delta \approx \delta_\gamma$).

A previous test in the vicinity of the trips (Rodríguez-López et al 2015b) shows that the spanwise uniformity in the mean profile is recovered at $x \approx 300\,\text{mm}$ for the cylinder case and at $x \approx 350\,\text{mm}$ for the sawtooth case. The closest measurement point in this study is located at $x = 446\,\text{mm}$, therefore it is ensured that there is no spanwise dependence in the points presented herein.

3 Results. One-point measurements

3.1 Integral parameters

Here the evolution of different integral parameters (momentum thickness, θ, and shape factor, $H = \delta^\star/\theta$) is investigated, where:

$$\delta^\star = \int_0^\delta \left(1 - \frac{u(y)}{u_e}\right) \mathrm{d}y \tag{2}$$

$$\theta = \int_0^\delta \frac{u(y)}{u_e}\left(1 - \frac{u(y)}{u_e}\right) \mathrm{d}y \tag{3}$$

We assume a linear interpolation between the first point and $y = 0$, $u = 0$. The main aim is to evaluate the gain in boundary-layer thickness presented by the different parameters for the two families of obstacles. In this first survey, all those trips summarized in table 1 were tested except the *2stag20* configuration. The obstacles were placed at $x = 160\,\text{mm}$ corresponding to $h/\delta_\gamma \gg 1$. In this part of the study, the closest point to the wall is acquired at $y_0 \approx 1\,\text{mm}$ for simplicity, thus not allowing consideration of inner variables.

Figure 4a shows the evolution of the thickness of the boundary-layer along the downstream distance x for the different obstacles. Both configurations with sawtooth trips seem to generate a thicker TBL than any of the cylinders used (even though $h_{Saw} < h_{Cyl}$). Both of the orientations tested for the sawtooth obstacle ($\pm 40°$ with the vertical) give similar results of thickness and shape factor, one can

(a) Momentum thickness, θ, evolution.

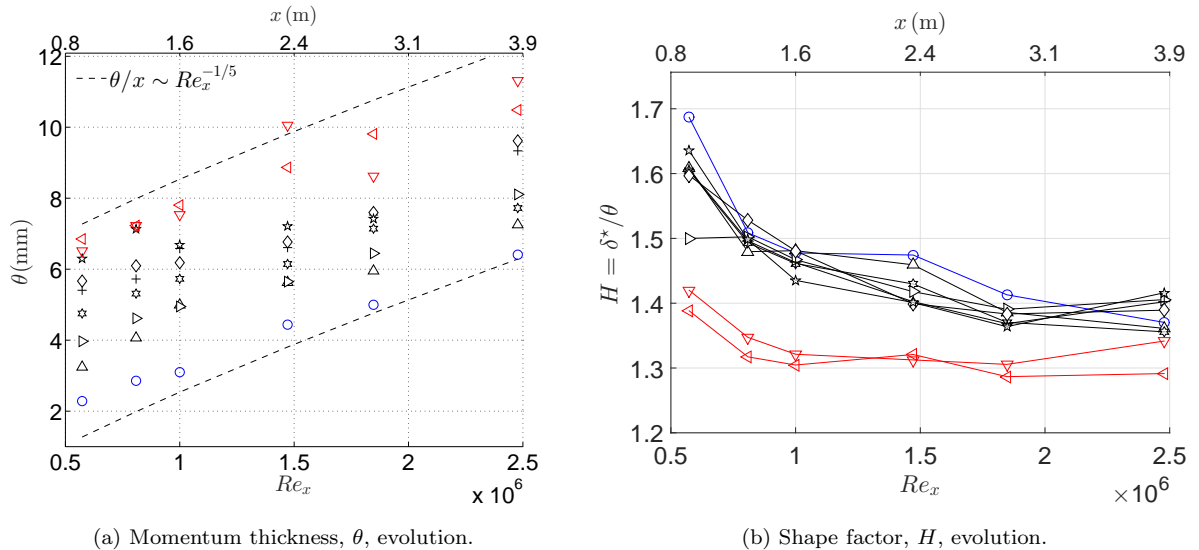(b) Shape factor, H, evolution.

Fig. 4: Evolution of integral parameters. Symbols are given in Table 1.

therefore conclude that this orientation is of little significance and in the following the *Saw Inv* trip will be discarded. Regarding the cylinders, the main effect shown is that the resultant thickness of the disturbed TBL depends on the height of the tallest cylinder more than the inclusion of a second row. In this line, we can observe that there are almost no differences between *10and20* and *20and10* obstacles and that they only produce a TBL thickness slightly different to *1row20* or *2row20*. Figure 4b is consistent with this trend where one can see that two clearly defined behaviours are presented. The shape factor of the *Saw* family presents a completely different tendency than the *Cyl* family which, at the same time, presents the same trend of the *Natural* case. It is clear from these results that two different behaviours can be distinguished depending on whether the obstacles are from the *Saw* or *Cyl* families. In the subsequent discussion, only the more representative members of each group (*2row20*, *2stag20* and *Saw*) will be tested in a more detailed study of the properties associated with the two families.

3.2 Freestream spectra

Note that the previous subsection has only studied the differences in the wake part of the boundary-layer (both θ and H are dominated by the behaviour of the outer regions). Such a clear modification of the outer part of the boundary-layer may have an influence on the freestream (laminar) fluid above the TBL.

Figure 5a shows the power spectral density (PSD) at $y/\theta = 19$ ($2 \leq y/\delta_{99} \leq 3$ indicating that no intermittency is present), it can be seen that the *Saw* family presents a significantly higher energy content at low frequencies. Note that at $y/\theta = 19$ the probe is well outside of the boundary-layer in a region where the flow is permanently irrotational, this peak should be seen, therefore, as the irrotational random motions of the potential flow outside of the turbulent not-turbulent interface of a boundary-layer (Phillips 1955), also reported for instance in Favre et al (1957). The physics behind this phenomenon can be explained briefly as follows: The boundary-layer is bounded from the freestream by a highly corrugated turbulent not-turbulent interface. For events where the instantaneous height of the turbulent not-turbulent interface is above its average position, the passage of the freestream is reduced in size and it is thus accelerated due to continuity. Similarly, instantaneous heights of the interface smaller than average require a freestream deceleration. This implies that the typical energy of this phenomenon is related to the difference between the maximum and the minimum heights of the turbulent not-turbulent interface for the two events described. If we consider the flow downstream of the trips, we can assume that this difference would be much bigger in the sawtooth case due to the recirculation downstream of the obstacle than in the cylinder case, where the flow remains more ordered. The decay of this perturbation with the wall normal distance (not shown for brevity) follows an exponential trend as demonstrated by Phillips (1955).

We can define as $St^\star$ the Strouhal number (based on the momentum thickness) where the maximum of this peak is located and then normalize the power spectral density at this particular frequency, $E_{11}(St = St^\star)$, with the one that the *Natural* case gives, $E_{11}^{Nat}(St = St^\star)$. Figure 5b shows that the *Saw* family
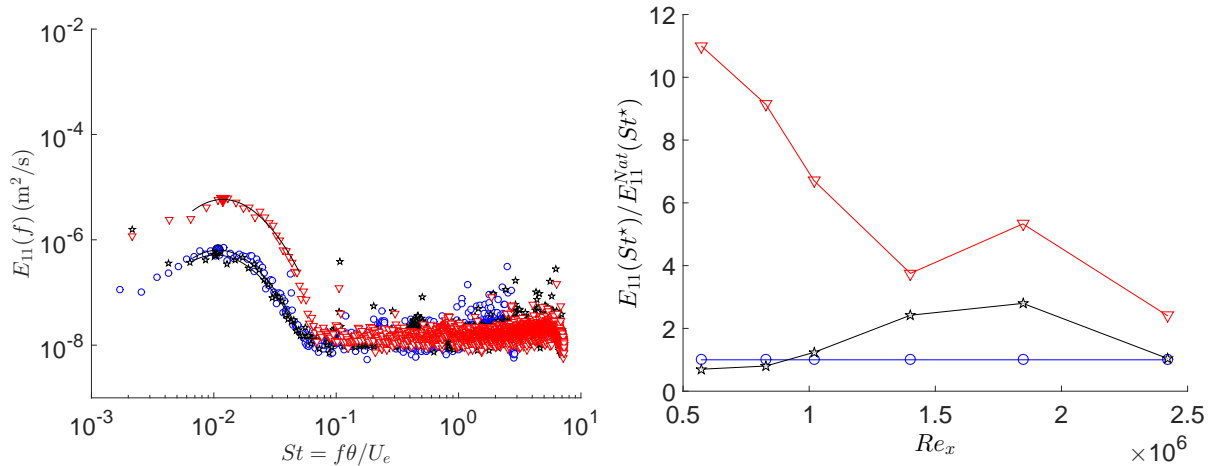
(a) Power density spectra, E_{11}, in the freestream at $y/\theta = 19$. Filled symbols show the maximum for each trip.

(b) Power spectral density, $E_{11}(St = St^\star)$, at $y/\theta = 19$ normalized with the Natural case.

Fig. 5: Power spectral density in the freestream. Symbols are given in Table 1.

presents a peak intensity up to 10 times stronger than the natural case, and this difference persists with increasing Re_x, meaning that the fluctuations present in the wake of these obstacles are considerably larger than the ones present for the *Cyl* case. This result supports the previous hypothesis of two different behaviours for the two distinct families of obstacles.

3.3 Diagnostic quantities. $\{C_f, \Pi, H\}$

In this section, results are presented for one point measurements with three different trips (*2row20*, *2stag20* and *Saw* described in table 1 representative of uniform and non-uniform distributions of blockage) located at $x_t = 160\,\text{mm}$ and $x_t = 890\,\text{mm}$ in order to simulate the different degrees of immersion in the TBL $h/\delta_\gamma \gg 1$ and $h/\delta_\gamma \approx 1$ respectively. The properties of the flow downstream of the trips will be assessed based on the evolution of three quantities, friction coefficient, C_f, wake component, Π (defined in equation 4), and shape factor, $H = \delta^\star/\theta$.

$$u^+ = u^+_{inner} + \frac{2\Pi}{\kappa}\mathcal{W}(\eta; \Pi) \tag{4a}$$

$$\mathcal{W}(\eta) = \frac{1 - \exp\left[-(1/4)(5a_2 + 6a_3 + 7a_4)\eta^4 + a_2\eta^5 + a_3\eta^6 + a_4\eta^7\right]}{1 - \exp\left[-(1/4)(a_2 + 2a_3 + 3a_4)\right]} \times \left(1 - \frac{1}{2\Pi}\ln(\eta)\right) \tag{4b}$$

$$\eta = y/\delta, \ a_2 = 132.8410, \ a_3 = -166.2041, \ a_4 = 71.9114 \tag{4c}$$

The evolution of the shear stress can be seen as an indicator of the degree of development present in the inner region of the TBL since this is the part of the flow with larger velocity gradients and turbulence production. Note that, although the accuracy on the determination of C_f is, at least, as good as any available independent measurement of u_τ, it is performed by fitting the experimental velocity profile to a canonical description. As such, in strongly disturbed cases, there is a risk that the method may artificially influence the velocity profile to follow the description that this profile has been fitted to. However, Rodríguez-López et al (2015a) demonstrated that this was not the case and that the method was highly robust even in mildly to strongly disturbed flows as the ones presents here. One should note as well, that the uncertainty on the determination of C_f decreases with x, both because the effect of the trips is diminished and because the Reynolds number (and hence the extent of the logarithmic layer) is larger.

The selection of the wake component, Π, and the shape factor, H, as diagnostic quantities is suggested first in Chauhan et al (2009) where they propose these two quantities because of their great sensitivity to different boundary or initial conditions. The quality test demanded from the velocity profiles is therefore more strict than the typical criteria required in extraordinarily thick (atmospheric) boundary-layers.

Figures 6 and 7 show three main results common for the evolution of these three quantities.
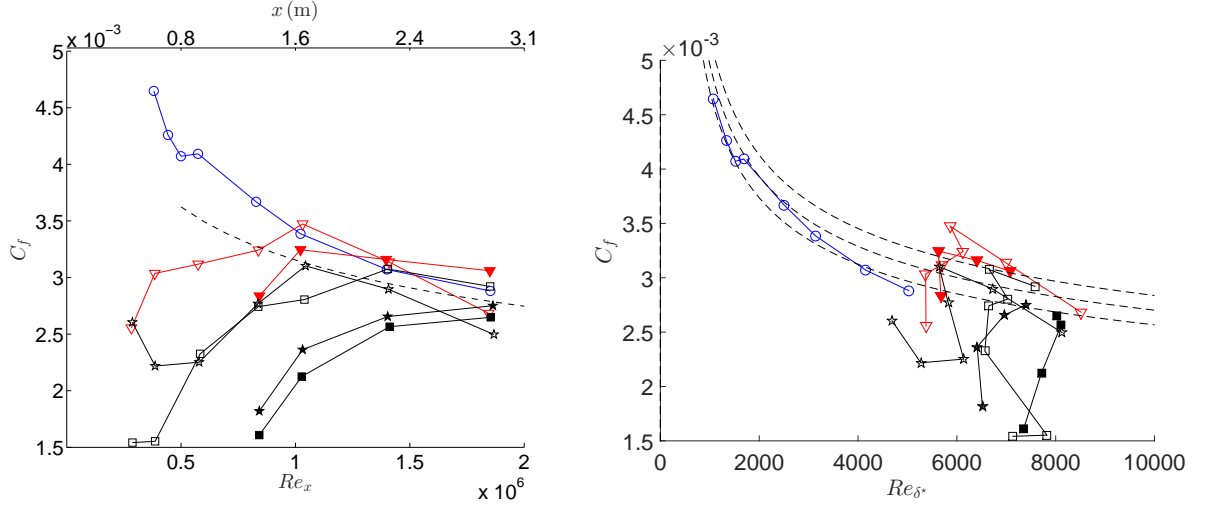
(a) $C_f = f(Re_x)$. Dashed line is given by $C_f = 0.058Re_x^{-1/5}$ (Nagib et al 2007).

(b) $C_f = f(Re_{\delta^\star})$. Dashed line is given by (Chauhan et al 2009).

Fig. 6: Evolution of the inner characterization variable (friction coefficient, C_f) in the one-point measurement experiment. Symbols are given in table 1. Empty symbols correspond to a trip location at $x_t = 160\,\mathrm{mm}$ where $h/\delta_\gamma \gg 1$. Measurements are taken at $x = \{0.446, 0.6, 0.9, 1.3, 1.6, 2.2, 2.9\}\,\mathrm{m}$. Filled symbols correspond to a trip location at $x_t = 890\,\mathrm{mm}$ where $h/\delta_\gamma \lesssim 1$. Measurements are taken at $x = \{1.3, 1.6, 2.2, 2.9\}\,\mathrm{m}$.
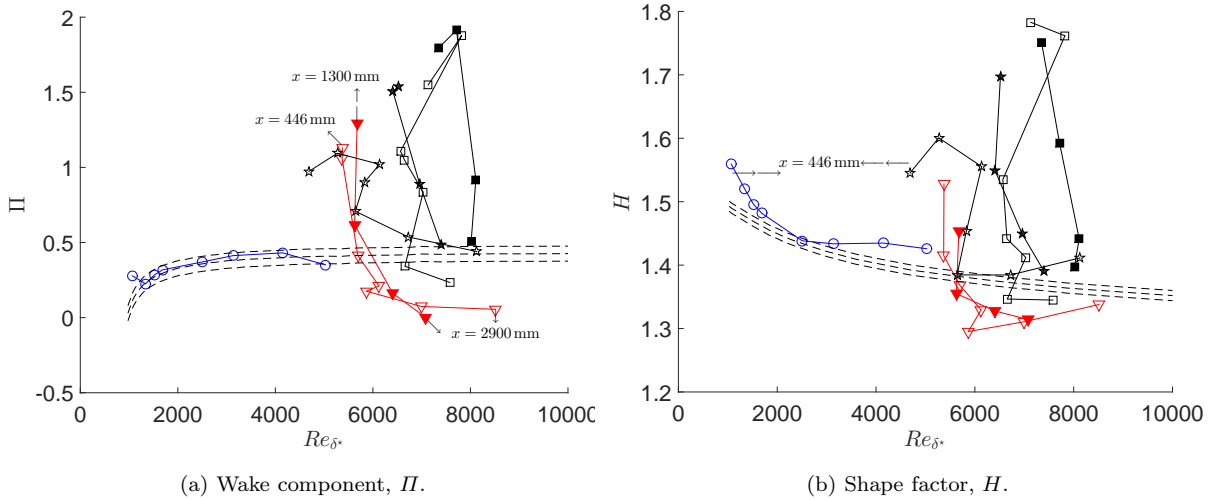
(a) Wake component, Π.

(b) Shape factor, H.

Fig. 7: Evolution of the outer characterization variables in one-point measurement experiment. Symbols are given in table 1. Empty symbols correspond to a trip location at $x_t = 160\,\mathrm{mm}$ where $h/\delta_\gamma \gg 1$. Measurements are taken at $x = \{0.446, 0.6, 0.9, 1.3, 1.6, 2.2, 2.9\}\,\mathrm{m}$. Filled symbols correspond to a trip location at $x_t = 890\,\mathrm{mm}$ where $h/\delta_\gamma \lesssim 1$. Measurements are taken at $x = \{1.3, 1.6, 2.2, 2.9\}\,\mathrm{m}$. Dashed lines are given by Chauhan et al (2009).

First, although not exactly the same, the evolution of the staggered configuration (*2stag20*) is similar to the original arrangement of cylinders (*2row20*). This result may be surprising since the projected frontal blockage ratio of *2stag20* is 60%, even bigger than the blockage of *Saw*. This is consistent with the previous observation that the important parameter is not only the blockage ratio but the distribution of it along the wall-normal direction. In particular, having 100% blockage for $y = 0$ may have an effect in the inner structures as will be discussed below. The bigger total blockage of *2stag20* is distributed for two different x locations generating a less severe disturbance in the near wall region. The behaviour of *2stag20* can be seen as an intermediate point between the other two trips as can be seen in the recovery values at the furthest downstream location for Π and H.

Second, downstream of any obstacle there is an adaptation region followed by a zone where the different quantities tend to follow the standard properties. The degree of recovery of the different magnitudes varies among the various obstacles used. The trend followed by the friction coefficient (related with the inner part of the boundary-layer) seems to be canonical even for the most strongly disturbed case (Saw). However, the more sensitive parameters (Π and H) show a greater departure from the canonical values for all cases. The poorer recovery of these properties for the Saw follows the same trend as shown in Sect. 3.2 since both quantities are related with the large distortion present in the wake.

Third, the distance from the obstacles is a more important parameter than the degree of immersion of the trips in the surrounding boundary-layer. One can see for instance that the points located at $x = 1.3\,\mathrm{m}$ ($Re_x \sim 8 \cdot 10^5$) for the advanced configuration of trips (filled symbols, $x_{trips} = 890\,\mathrm{mm}$) show similar C_f, H and Π than the results for $x = 0.6\,\mathrm{m}$ ($Re_x \sim 3.8 \cdot 10^5$) for the standard configuration (empty symbols, $x_{trips} = 160\,\mathrm{mm}$). One possible explanation would be that both points present a similar distance $\tilde{x} \approx 400\,\mathrm{mm}$ from the obstacle to the measurement point. Therefore one can conclude that the degree of immersion in the boundary-layer (for the tested configurations) is less important than the distance from the obstacles, $\tilde{x}$.

It has been reported that Π provides a measurement of the degree of distortion of the outer part of the TBL (Chauhan et al 2009). This distortion is not only more sensitive to external perturbations and changes in the boundary conditions, but also is known to have a bigger memory in the sense that it needs longer recovery distances to forget upstream disturbances (e.g. Simens et al (2009); Chauhan et al (2009) amongst many others). One may also consider the wake component as a measure of the size of the outer part of the boundary-layer. In this context all of the obstacles examined in this study present an artificially high wake component near the trips (meaning a larger physical wake) which then decreases progressively towards the natural case. In the case of $2row20$, the natural trend is practically recovered after $x \approx 2\,\mathrm{m}$. However, in the case of Saw the wake component keeps decreasing and does not recover the natural case up to the furthest location measured. Note that, as mentioned before, the behaviour of $2stag20$ seems to converge to an intermediate value between Saw and $2row20$ for the last measurement points.

Similar results are seen for the evolution of the shape factor given in Fig. 7b. A comment has to be made in the last 3 measurement stations for each of the test cases, these points follow an increasing trend, probably due to the slightly positive pressure gradient present in this zone (Fig. 2a). The presence of this pressure gradient makes it difficult to determine whether the departure from the expected trend for $2row20$ together with the tendency of Saw towards the value proposed by Chauhan et al (2009) are genuine effects of the trips or an artefact of the pressure gradient. One should be similarly cautious in examining the recovery of the shape factor for the various test cases. A similar trend is shown in Fig. 6b, where one can see that the furthest points (also for the natural case) tend to deviate towards smaller friction coefficients than expected. This effect is correspondent to a slightly adverse pressure gradient, hence it supports the idea that the deviation present for the trend of the shape factor is also due to a small adverse pressure gradient.

Summarizing, after a highly distorted region which can be seen as an adaptation period downstream of the obstacles, the one-point properties of the flow tend to the natural case. This recovery is faster and more canonical in the case of the cylinders ($2row20$) than in the Saw which does not recover the natural properties of the TBL. Effects such as the degree of immersion in the boundary-layer and the overall blockage (simulated staggering the downstream row of cylinders) seem to be less relevant than the downstream distance from the trips, which appears to play a dominant role. Thus, three main behaviours can be outlined, the $Natural$ case, wall-normal constant blockage ($2row20$) and non-uniform distribution of wall-normal blockage (Saw).

Table 2 shows the values of different Reynolds numbers for various downstream positions and trips. On it, one can see that the thickness of the boundary-layer (and equivalently the Reynolds number) is increased. If we consider the latest downstream position $2row20$ trips present a thickness 153% of that of the $Natural$ case for the same downstream position which corresponds to a 43 and 63% increase in Re_τ and Re_θ respectively.

3.4 Velocity profiles

The evolution of the mean and fluctuating velocity profiles (including spectra) in each test case has been studied. Figures 8 and 9 show the evolution of those three quantities along the downstream distance for the three different behaviours identified above.

x (m)		0.446	0.6	0.9	1.3	1.6	2.2	2.9
	Natural		368	556	803	925	1159	1435
Re_τ	*2row20*	918	846	1055	1314	1572	1890	2064
	Saw	1028	1332	1800	2413	2656	2985	3133
	Natural		686	1138	1741	2189	2894	3526
Re_θ	*2row20*	3034	3293	3946	4010	4073	4858	5757
	Saw	3518	3794	4158	4608	4530	5337	6363
	Natural		12.0	19.2	29.4	35.2	46.5	59.2
δ (mm)	*2row20*	39.5	39.4	48.9	54.9	61.1	77.7	90.7
	Saw	45.3	53.3	71.4	93.0	98.8	117.6	134.5
	Natural		31	29	27	26	25	24
l_w^+	*2row20*	23	21	22	24	26	24	23
	Saw	23	25	25	26	27	25	23

Table 2: Evolution of various parameters of the flow with downstream distance.

(a) $x = 0.6$ m

(b) $x = 0.9$ m

(c) $x = 1.3$ m

(d) $x = 1.6$ m

(e) $x = 2.2$ m

(f) $x = 2.9$ m
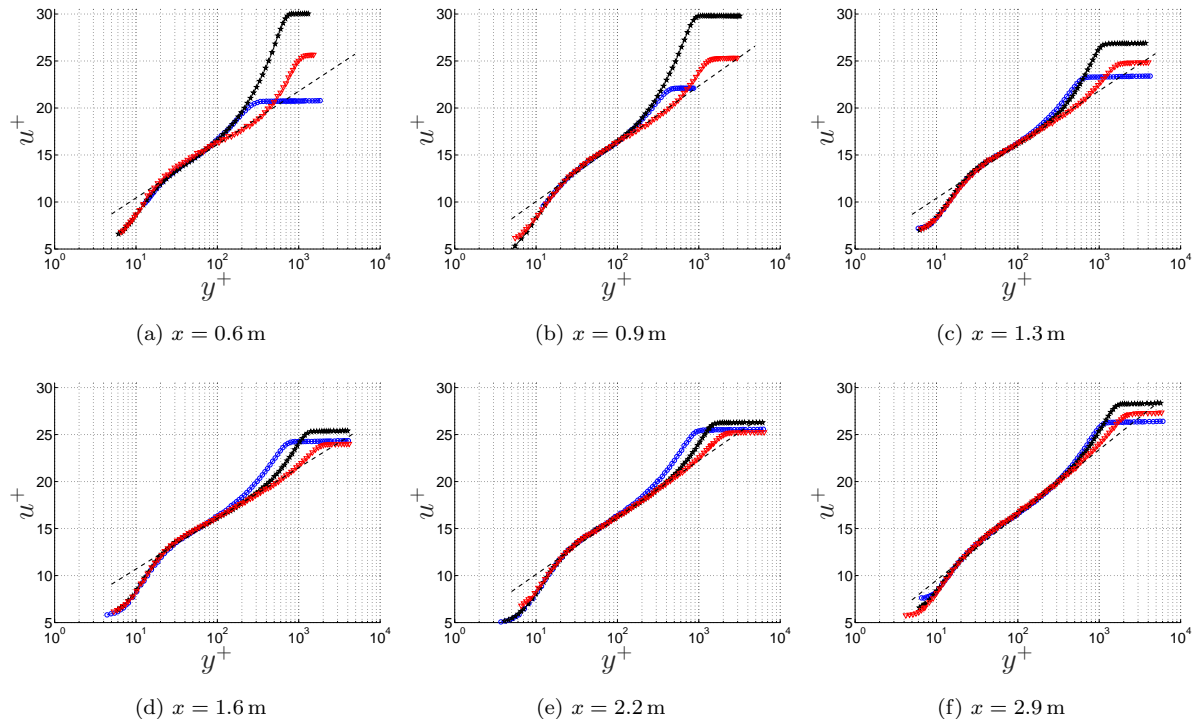
Fig. 8: Mean velocity profile for *Natural*($\circ$), *2row20*($\star$) and *Saw*($\triangledown$) at different downstream positions. Dashed line marks the logarithmic law $u^+ = \frac{1}{\kappa}\log(y^+) + B$.

Mean velocity u^+. In all cases, in the most upstream locations, closest to the trips, an artificially larger wake is present which eventually decreases until the natural trend is recovered. Given the relatively high Reynolds number of these flows, the extent of the logarithmic law is very small for the disturbed cases in $x = \{0.446, 0.6, 0.9\}$ m. This is attributed to the flow being formed primarily of the wakes from the trips rather than being a genuine TBL. It is worth noting that, although all the other properties for the *Saw* case do not follow the canonical case, the appearance of the logarithmic layer for the mean profile shows notably good agreement with the logarithmic law of the natural case. A question might arise here regarding whether this agreement is an artefact of the friction velocity u_τ and the wall-probe relative position being extrapolated from a comparison with the canonical mean velocity profile. However, a closer inspection of the three profiles for $x > 1.5$ m seems to show that indeed they appear to have a smaller wake than expected, as shown also by Fig. 7a. Note also that, after the adaptation region, the *2row20* case generates a boundary-layer of 163% higher Reynolds number based on the momentum thickness, $Re_\theta = \theta u_e/\nu$.

Variance u'^+. There are three outstanding features in the turbulence intensity profiles. First, the magnitude of the inner peak is seen to increase with x for the latest measurement points in the disturbed

cases and for every location in the *Natural* case. This is a combined effect between the well known lack of spatial resolution of hot-wires when etched to the same length (in mm) which entails a different length (in viscous units) for the various downstream positions (Hutchins et al 2009) and the Reynolds number (increasing magnitude of the inner peak as Re_τ increases). The values of l_w^+ are tabulated in Table 2. Second, the inner part of the boundary-layer in the cylinders case (*2row20*) is almost not disturbed by the presence of the obstacles (at the downstream positions measured) and the intensity of the inner peak of turbulence intensity (at $y^+ \approx 15$) presents similar values to the natural case for the same x. However, the tip vortices created by the cylinders at their tips have a significant influence on the flow up to $\tilde{x} \approx 250D$ downstream of the obstacles. Third, the *Saw* initially generates an artificially high turbulence intensity which then decreases with x to increase again after the adaptation region. This may be due to the recirculation appearing downstream of the obstacles which contributes to the flow with eddies of different sizes and a higher intensity over a greater wall-normal extent, in contrast to the *2row20* where the turbulence distortion generated by the cylinders was concentrated in the tip vortex.

Spectra. Figure 9 shows contours of pre-multiplied spectra normalized with the friction velocity, i.e. $E_{11}k/u_\tau^2$. This allows a direct equivalence between the area below the curve and energy contained. Assuming Taylor hypothesis for the convection velocity, $u_c(y) = u(y)$, a length scale is defined for each frequency, f, as $\lambda = u_c/f$, which in wall units results $\lambda^+ = \lambda u_\tau/\nu$. The natural case follows the expected trend with Reynolds number: At low Re there is just one scale in the flow associated with the inner peak (collapsing at $y^+ = 15$ and $\lambda^+ = 1000$ as mentioned in Marusic et al (2010) for instance) and the production of turbulent kinetic energy near the wall. With increasing Re the separation of scales becomes more evident leading to an external zone of high energy content located around $y/\delta \sim 0.06$ i.e. the middle of the logarithmic law (Marusic et al 2010). In the case of the distorted boundary-layer two different behaviours are present. First, the *2row20* does not modify the inner structures which appears to be consistent with the natural case for equivalent Re (same wall normal location as well as same characteristic length scale). The outer structures on the other hand, present a clearly defined peak at $y/h \sim 1$ corresponding to the tip vortex. This peak disappears after the adaptation region, downstream of which, due to the higher Re, the separation of scales becomes more clear than the natural case. Finally, the *Saw* produces a spectrum that is broadband in y in the closest locations to the trips, probably due to a combination of flow recirculation and tip vortices. This broadband energy is attenuated with increasing x, and gives place to a flow with similar spectral properties to the natural case. Note that the inner peak develops at a higher length scale for the *Saw* case (relative to the natural one).

3.5 Discussion

The appearance of the inner peak (and more particularly its lack of appearance in the *Saw* case) may give an idea about the formation mechanism of the boundary-layer acting behind various trips. On one hand, the cylinders, distort the outer part of the boundary-layer with a higher wake component. The inner structures recover after the trips fast enough so that at the first measurement point they appear to be almost unperturbed (Fig. 9 $x = 0.446$ m and $x = 0.6$ m). One possible physical explanation would be that the TBL grows entraining this outer fluid but the mechanisms of production of turbulence seem to be unaltered (as shown by the spectra). On the other hand, the sawtooth appears to generate an outer flow with high turbulence intensity. It also destroys the inner structures of the boundary-layer (note that the blockage of the sawtooth for $y = 0$ is 100%); these inner structures take some time to recover and, when they do, the length scale at which the maximum energy is observed for $y^+ = 15$ does not collapse at $\lambda^+ = 1000$ (Fig. 9 $x = 0.446$ m, $x = 0.6$ m and $x = 0.9$ m). The different length scale at which the inner peak appears in the first place suggests that this peak is more influenced by the outer fluid than by the inner structures and the wall. A clarification point has to be made regarding the appearance of the inner peak in the *Saw* case. The lack of inner peak that has been discussed does not mean that the energy content at $y^+ = 15$ $\lambda^+ = 1000$ is zero, it means that the strongest energetic contribution is not located at that length scale but at a higher $\lambda^+ \approx 2000$ receiving a high influence of the wake, and it is not until $x = 1.3$ m that the highest energy content in the near wall regions is located at the correct λ^+ meaning that it is not until that point where the inner dynamics of the boundary-layer are recovered. Note in particular that the energy introduced by the tip vortices in the *2row20* case remains at $y/h \approx 1$ contrasting with the broadband spectra present for the *Saw* for every y, that is, there is an influence of the outer part of the boundary-layer in the inner motions. These two different behaviours may be seen as two distinct formation mechanisms: one dominated by the wall structures growing and entraining fluid
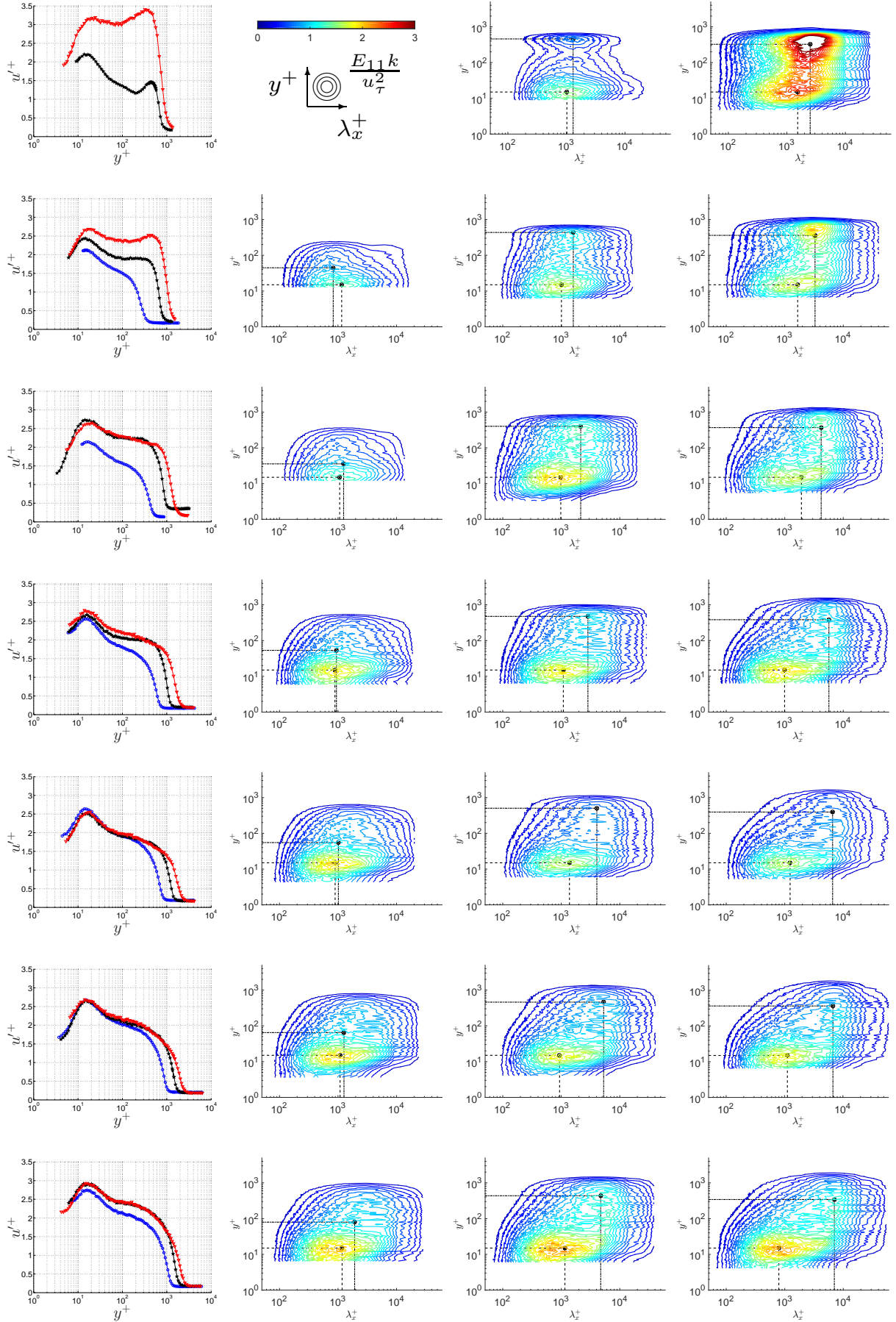
Fig. 9: Profiles of u'^+ (first column, symbols in Table 1) and contours of normalized premultiplied spectra $E_{11}k/u_\tau^2$ for *Natural* (second column), *2row20* (third column) and *Saw* (fourth column) at $x = \{0.446, 0.6, 0.9, 1.3, 1.6, 2.2, 2.9\}$ m from first to last row. Contour levels are from 0.2 in steps of 0.1. Dashed line shows $y^+ = 15$ and dashed-dotted line marks the middle of the logarithmic layer (*Natural*) or the height of the trip (*2row20* and *Saw*).

above the TBL (*wall-driven*) and the other featuring highly turbulent structures produced by the trips and not attached to the wall (*wake-driven*). The latter of these appears to have a reduced influence on the near-wall region which decays after an initial adaptation region. In particular, the flow in the vicinity of the trips presents a high importance, and possibly, the two mechanisms of formation of the boundary-layer are related with the aspect ratio of the obstacles, in this way, a shedding of vortices with wall normal vorticity (high aspect ratio) would cause little outer-inner interaction (*wall-driven* mechanism). On the contrary, shed vortices with vorticity in z, i.e. the recirculation-like structures present for the *Saw* case and also reported in Alving and Fernholz (1996) and Castro and Epik (1998), would enhance the wake influence on the wall generating a *wake-driven* mechanism.

The existence (or not) of these two different formation mechanisms behind the distinct trips motivates the next section. In it, two-point simultaneous measurements are taken to explore in more detail how the outer and the inner structures of the TBL interact with each other. It aims to answer the questions related with the eddy structure of the different boundary-layers generated by various obstacles as well as the formation mechanisms behind them.

4 Results. Two-point measurements

The correlations, both in the wall-normal and spanwise directions, between the two simultaneously sampled hot-wires will be studied in this section. The experimental set-up is as described in Sect. 2.2. This study will provide information about the eddy structure present in the TBL and how this structure might have been influenced by different formation mechanisms.

4.1 Wall-normal correlations

The wall-normal space-time correlation coefficient can be defined as

$$\rho(y,\tau) = \frac{\int_0^\infty u_0'(y_0,t)u_1'(y,t+\tau)\mathrm{d}t}{rms(u_0')rms(u_1')} \tag{5}$$

where u_0' and u_1' are the fluctuating velocity signals from the wall hot-wire (fixed at $6 \leq y_0^+ \leq 9$) and free hot-wire (at the same x_0 and z_0 and traversed in y) respectively. For a given y/δ the correlation coefficient presents a peak at a certain time delay $\tau \neq 0$ meaning that there is a preferential phase lag between both sensors (Fig. 10a). Using the frozen flow-field hypothesis (Taylor 1938) one can define a pseudo-streamwise coordinate $\hat{x} = \tau u_1$ where $u_1 = u_1(y)$ is the mean velocity measured by the free hot-wire. In order to focus on the shape of the correlations, these are going to be corrected by the time delay providing the maximum correlation, $\hat{x}_{max}$. As shown in Fig. 10b the correlations present a similar shape for the different trips at a given wall-normal distance perhaps with a slightly worse collapse in the *Saw* case but within the expected uncertainty. The points closer to the wall do not collapse as well as further from the wall probably due to the probe-probe interaction locally increasing the blockage.

Considering now the time delay which maximizes the correlation coefficient, τ_{max}, assuming the mean inclination of a fluid structure one can define the angle

$$\alpha(y) = \tan^{-1}\left(\frac{\tau_{max}u_1(y)}{\Delta y}\right) \tag{6}$$

where the symbols and a sketch is given in Fig. 11a. Results shown in Fig. 11b for the correlations presented above show $14° \leq \alpha \leq 18°$ without any clear trend depending on the trip used. This result is in a good agreement with previous studies such $\alpha = 18°$ by Brown and Thomas (1977), $\alpha = 16°$ by Robinson (1986), $\alpha = 15°$ by Boppe et al (1999) or $\alpha = 14°$ by Marusic and Heuer (2007). Note that, for brevity, results are only shown for the highest Re, i.e. $x = 3.9\,\mathrm{m}$; at which point, both the angle and the correlation coefficient curves have overcome an adaptation process downstream of the trips. The main result is that there are not significant differences (except the poorer collapse of ρ for the *Saw* case) for the distinct obstacles meaning that the wall normal structure does not change for the different formation mechanisms. However, the slight divergence for ρ in the *Saw* case shown in Fig. 10b could imply a structural change in the eddy organization of the TBL and should be studied in more detail.

In order to provide a better explanation of the phenomena shown above, one can study in more detail the wall structure by using the normalized cross power spectral density defined as

$$\Gamma = \frac{\|cpsd(u_0',u_1')\|^2}{psd(u_0')psd(u_1')} \tag{7}$$

(a) Correlation coefficient, ρ, at $x = 3.9\,\mathrm{m}$ (b) Corrected correlation coefficient, ρ, at $x = 3.9\,\mathrm{m}$
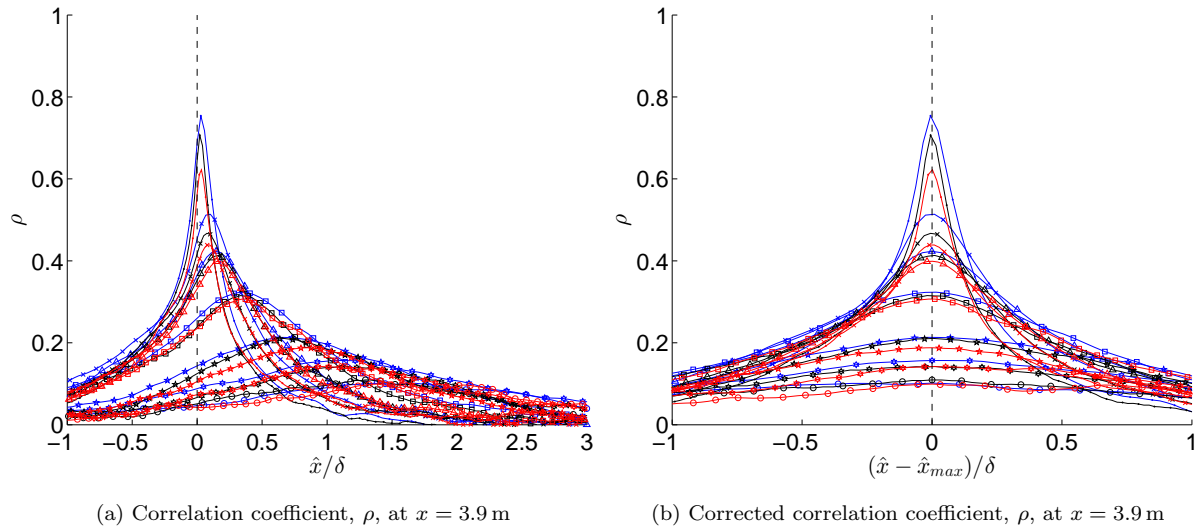
Fig. 10: Correlation coefficient, ρ, at different wall normal locations and for various trips. Symbols mean $\{\cdot \times \triangle \square \star \ast \circ\} \to y/\delta = \{0.01, 0.03, 0.05, 0.1, 0.2, 0.3, 0.4\}$. Colours mean $\{blue,\ black,\ red\} \to \{Natural,\ 2row20,\ Saw\}$.

(a) Sketch and parameters of eddy structure and inclination (b) Mean structure angle, α for different trips at $x = 3.9\,\mathrm{m}$
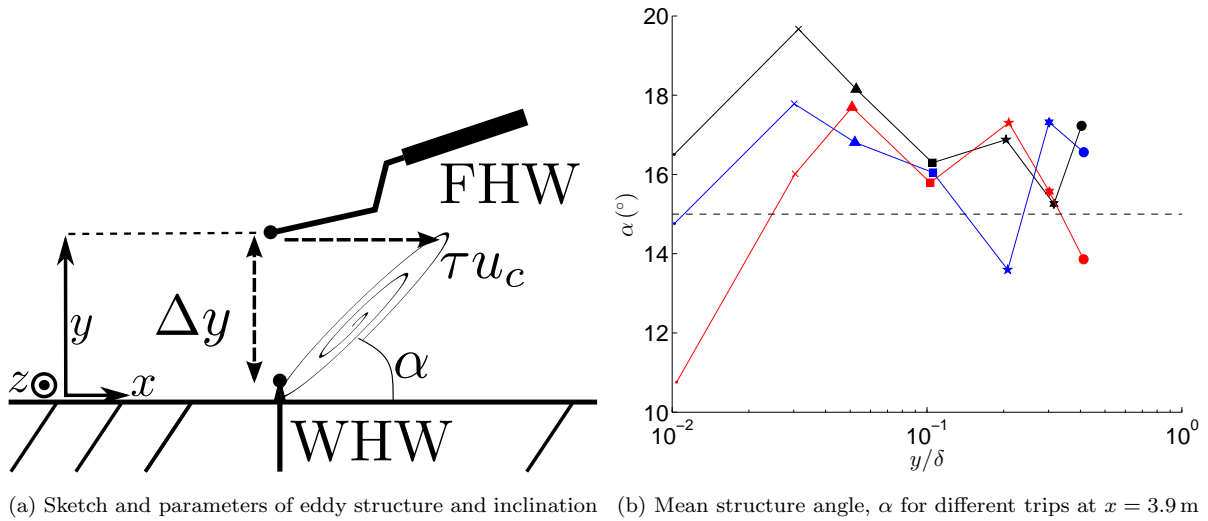
Fig. 11: Mean structure inclination angle, α, at different wall normal locations and for various trips. Symbols mean $\{\cdot + \triangle \square \star \ast \circ\} \to y/\delta = \{0.01, 0.03, 0.05, 0.1, 0.2, 0.3, 0.4\}$. Colours mean $\{blue,\ black,\ red\} = \{Natural,\ 2row20,\ Saw\}$.

It allows the evaluation of the correlation at a given frequency (the frequency domain is chosen over the wave number domain to avoid any debate over the convection velocity in this section) between two points separated by distance $\Delta y = y - y_0$. For a given frequency, it is evident that Γ should decrease with increasing separation. Let us consider the CPSD at a height y over the wall, this correlation would vanish for eddies (frequencies) of a size $d^\star$ ($f^\star$ in the frequency domain). One could then consider how this size ($d^\star$ or $f^\star$) scales with the wall-normal coordinate, in particular whether it grows linearly with y as predicted by the attached eddy model of Townsend (1976). If this is the case, it should follow that the contours of constant correlation level, Γ, should be located over a line $d^\star \propto y \to f^\star \propto 1/y$, or equivalently, appear at a constant $y \cdot f$ for every y, at least in the self-similar region.

Figure 12 shows plots of cross power spectral density for each of the test cases considered. One can see that in the *Natural* case the contours present a clear vertical region corresponding approximately with the extent of the logarithmic layer, this vertical tendency, associated with the attached eddy hypothesis as discussed above, is present also in the *2row20* case (perhaps less defined but always within the assumed uncertainty) and it presents a clear departure in the *Saw* case where the curves form an angle with the vertical. Thus it follows that, although the mean inclination of the eddy structures towards the wall

appears to be unaltered for the different obstacles, the organization of the eddies inside the TBL differs clearly from the canonical case to the *Saw* case. Note that contrary to other properties shown in previous sections, this effect lasts up to the furthest measurement point ($x = 3.9$ m), it may suggest, therefore, that it is linked with the actual formation mechanism of the turbulence rather than with some kind of adaptation process from the obstacles as hypothesised before as the *wake-driven* mechanism.
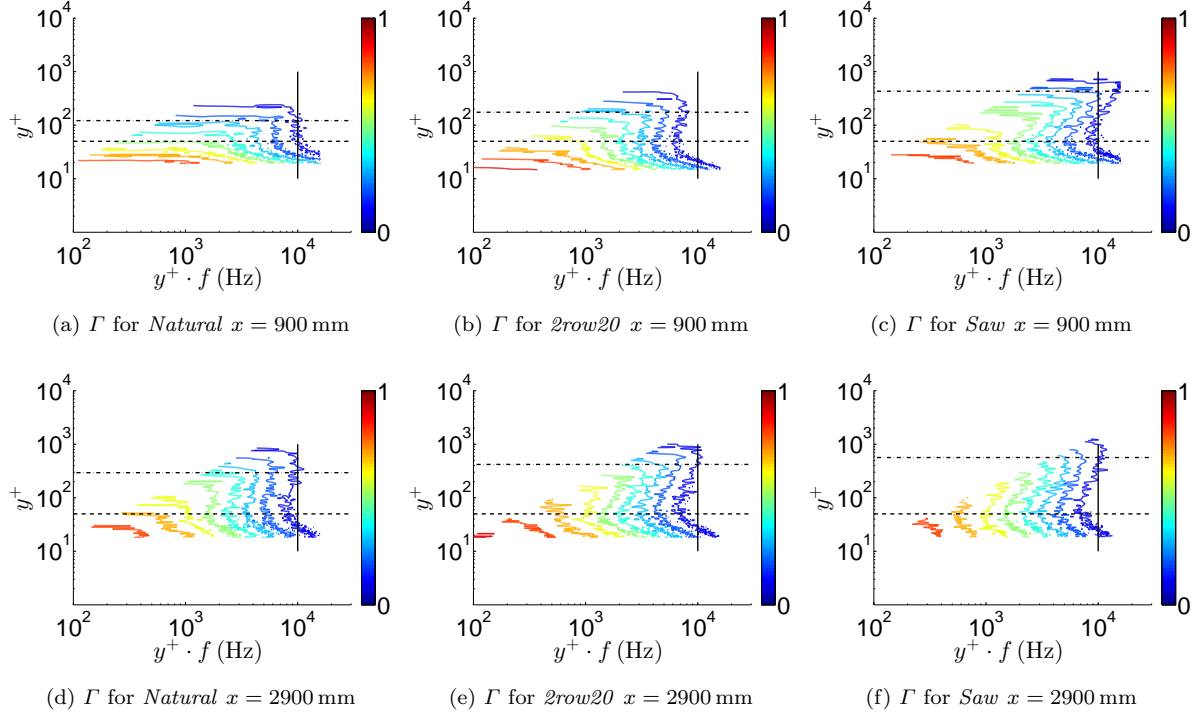

Fig. 12: Normalized cross power spectral density, Γ, for different trips and different downstream positions. Contours are given from 0.1 to 0.9 in steps of 0.1. Dashed ($--$) and dash-dotted ($-\cdot-\cdot$) lines corresponds to the limits of the logarithmic layer. Solid vertical line shows a reference in order to help the visualization of the self-similar region

4.2 Spanwise correlations

The homogeneity and the wall structure in the spanwise direction are tested by means of the time averaged correlation coefficient, ρ, defined as the correlation between the fluctuating velocities u'_0 of the wall hot-wire (fixed at height y_0 and spanwise position z_0) and u'_1 of the free hot-wire (fixed at the same height y_0 and moving along z). Since in this case, contrary to the previous section, both hot-wires are located at the same y one should not account for an inclination angle and therefore the correlation coefficients are taken as a function only of z with a null time delay. The two wall normal locations chosen were $y \approx 0.25$ mm (corresponding to $6 \leq y^+ \leq 9$ for the different cases) and $y \approx 3.5$ mm (the maximum available height for the wall hot-wire corresponding to $60 \lesssim y^+ \lesssim 110$), thus belonging to the logarithmic layer.

Results are presented in Fig. 13 for the two heights tested, belonging to the buffer and logarithmic layer respectively. Although one could expect the lateral correlation in the buffer layer to scale in inner variables, Fig. 13a shows that the different curves collapse clearly in outer scaling at least for the *Natural* case. It could be argued that the *2row20* trend also follows the natural case closer than the *Saw* case but the correlation level is so low that the uncertainty makes this somewhat speculative. Note as well that the geometrical configuration of the hot-wires, in particular their prong to prong distance (3 mm $\gtrsim 100\,\delta_\nu$) makes it almost impossible to detect wall streaks separated by around 100 wall units (Adrian 2007).

The results in the logarithmic layer makes the previous argument clearer, Fig. 13b confirms that the trend followed by the *Saw* differs from that presented by *2row20*, which follows the *Natural* tendency. It also shows clearly the undershoot below $\rho = 0$ indicative of region of fluctuating velocity flanked by
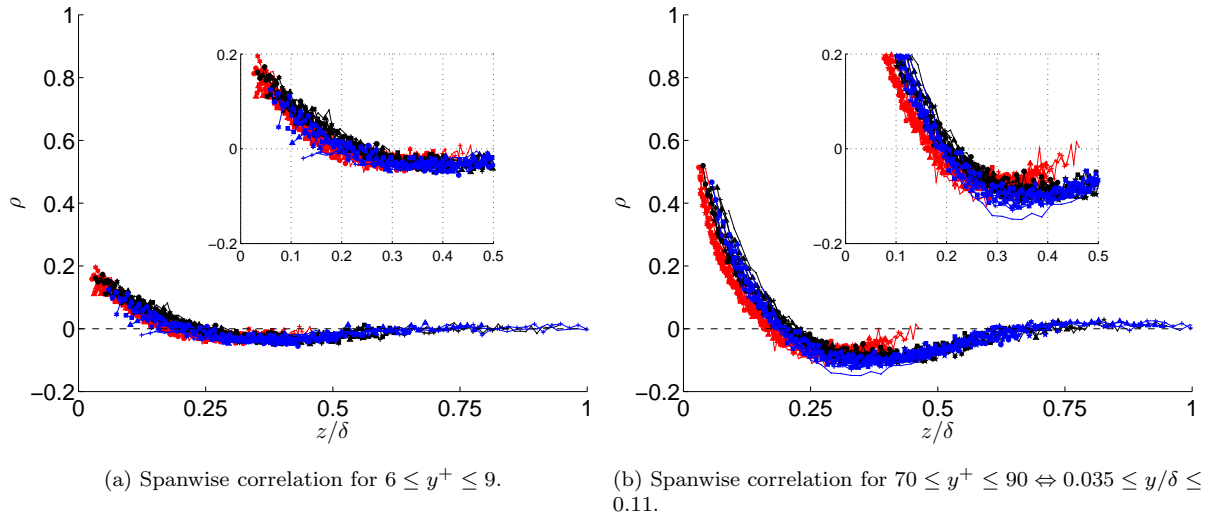
(a) Spanwise correlation for $6 \leq y^+ \leq 9$.

(b) Spanwise correlation for $70 \leq y^+ \leq 90 \Leftrightarrow 0.035 \leq y/\delta \leq 0.11$.

Fig. 13: Spanwise correlation coefficient, ρ, for various trips (blue=*Natural*, black=*2row20*, red=*Saw*). Symbols mean $\{\cdot + \triangle \square \star \ast \circ\} \rightarrow x = \{0.9, 1.1, 1.5, 1.9, 2.4, 3, 3.9\}$m

regions of the opposite sign. These features have been associated with the meandering of the superstructures resident in the logarithmic layer (Hutchins and Marusic 2007a). The value of the correlation is also bigger than in the buffer layer, in particular, one would expect at this height ($y \approx 3.5\,\text{mm}$) eddies of a similar size (which also is the typical initial separation of both hot-wires) therefore providing a higher correlation value contrary to the buffer layer (where eddies are expected to be much smaller than the initial separation of the hot-wires).

These results show that there is not any artificial spanwise periodicity introduced by the obstacles (note from table 2 that δ triples in the streamwise extent considered while the spanwise periodicity of the obstacles remain constant). However, they also show that the *Saw* presents a different eddy structure (at least in the logarithmic layer). This should not be wrongly attributed to a transient process from the trips since it scales with outer variables for every x considered. It may be not very surprising that a wake-driven mechanism as the one suggested for the *Saw* scales in outer variables. However, it appears strikingly clear that the wall structure, even in the *Natural* case, collapses in outer variables as close to the wall as the buffer layer. This result was reported previously by Hutchins and Marusic (2007a) for $y/\delta = 0.05$ but not so close to the wall. It can be explained by the modulation and superposition of the superstructures resident in the logarithmic layer in the inner region (which will be studied in the next section).

Summarizing, the spanwise organization of eddies scales for every case in outer variables as close to the wall as the buffer layer. The negative correlation present shows the appearance of regions of fluctuating velocity flanked by opposite sign fluctuations which spanwise extent seems to collapse in outer variables. The fact that the *Saw* case presents scaling in outer variables which is clearly different from that of *Natural* and *2row20* (who also scale as y/δ but they do not collapse with the *Saw* case) suggests a different organized motion which is not simply an artifact of an adaptation region from the trips.

4.3 Modulation

The interaction between the outer and inner regions of the boundary-layers has always been a topic of research interest, for instance the concept of inactive motions of Townsend (1976), some of the results shown by Brown and Thomas (1977) also suggest this kind of interaction, or the mixed inner-outer scaling proposed by DeGraaf and Eaton (2000) among many others. This interest has been intensified in the last few years since the proposal of a modulation mechanism of the inner scales by the outer motions as being responsible for this interaction (Hutchins and Marusic 2007b). This modulation coefficient can be measured (Mathis et al 2009) and it allows the extrapolation of inner variables for a given outer flow (Mathis et al 2011; Marusic et al 2011; Mathis et al 2013). It is also the subject of ongoing studies developing a theoretical model for this phenomenon (Chernyshenko et al 2012). This tool also provides an excellent instrument to quantify the outer-inner interaction present for the different obstacles.
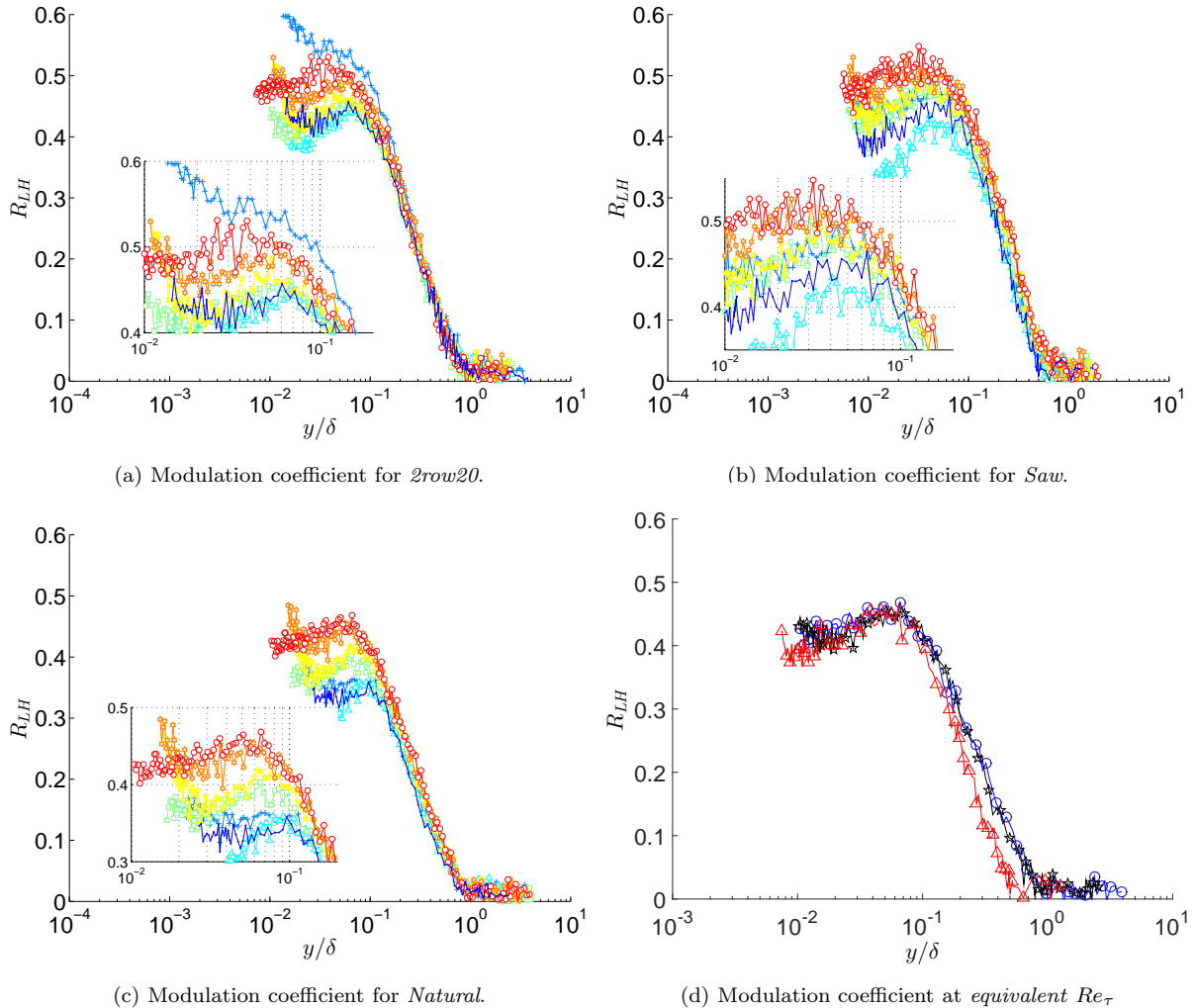
(a) Modulation coefficient for *2row20*.

(b) Modulation coefficient for *Saw*.

(c) Modulation coefficient for *Natural*.

(d) Modulation coefficient at *equivalent* Re_τ

Fig. 14: Evolution of the modulation coefficient, R_{LH}, for various trips, symbols mean $\{\cdot + \triangle \square \star * \circ\} \rightarrow$ $x = \{0.9, 1.1, 1.5, 1.9, 2.4, 3, 3.9\}$m in plots $a - c$ and $\{\circ \star \triangle\} = \{$*Natural, 2row20, Saw*$\}$ in plot d.

A brief description of the method used is as follows: The fluctuating velocity, u'_0 of the wall hot-wire (fixed in the buffer layer) is low-pass filtered at a filter length $\lambda_f = \delta$ (assuming Taylor's hypothesis for the convection velocity) resulting in the large and small component fluctuations u'^L_0 and u'^H_0 respectively, where $u'^L_0 + u'^H_0 = u'_0$. The same filter is applied to the fluctuating velocity $u'_1 = u'^L_1 + u'^H_1$ of the free hot-wire (at the same x_0 and z_0 of the wall hot-wire and traversed in y). The amplitude of the small scale fluctuations will be taken as the envelope of the high frequency signal calculated by means of the Hilbert transform, as suggested by Mathis et al (2009), resulting in $\mathcal{H}(u'^H_0)$. The envelope is then low-pass filtered at the same frequency, $\mathcal{H}^L(u'^H_0)$, in order to avoid the contribution of the small scales to the large scale envelope. One can then define the degree of modulation as the correlation between the large scales of the outer sensor and the envelope of the small scales in the buffer layer:

$$R_{LH} = \frac{\overline{u'^L_1 \mathcal{H}^L(u'^H_0)}}{rms(u'^L_1) rms(\mathcal{H}^L(u'^H_0))} \tag{8}$$

Results of the modulation coefficient are shown in Fig. 14 for the different trips and the measured downstream locations. They suggest that the modulation coefficient has a plateau in the buffer and logarithmic layers followed by a drop to zero in the outer region which collapses in outer scaling. The magnitude of the plateau (amplified in the insets) seems to increase with increasing Re, as suggested by Mathis et al (2009) amongst others, meaning that the influence of the outer structures in the inner regions is more accentuated when a bigger separation of scales is present. Note that the two most upstream locations for the disturbed cases do not follow this trend, probably because of an influence of the trips. There is an extraordinarily high modulation present at $x = 1.1$ m for the *2row20* case. It could

be explained as an effect of the proximity of the trips, but this might be inconsistent with the smaller modulation at $x = 0.9$ m thus it seems difficult to extract a clear conclusion. Another explanation for this fact could be the distribution of the spectral energy. The employed filter ($\lambda_f = \delta \rightleftarrows \lambda_f^+ = Re_\tau$) assumes that the inner peak ($y^+ = 15$, $\lambda^+ = 1000$) is part of the small scales if and only if $Re_\tau > 1000$. One can see in Fig. 9 that for $x \approx 1$ m (where $Re_\tau \approx 1000$) part of the energy of the inner peak is at $\lambda > \lambda_f$ and part is $\lambda < \lambda_f$; this effect may generate an artificially large modulation due to the insufficient separation of scales.

In order to compare the effect of the Reynolds number, a selection is made of the different experiments which present an *equivalent* Reynolds number, that is: $Re_\tau^{Natural} = 1732$; $Re_\tau^{2row20} = 1686$; $Re_\tau^{Saw} = 2538$. The last value being the minimum (and therefore closest to the trips) value among the measured ones. Figure 14d shows that the *2row20* and *Natural* cases collapses accurately both in the magnitude of the plateau and in the outer decay region. On the other hand the *Saw* presents a different behaviour in the outer part, the question whether this change of behaviour appears because the measurement location is not far enough from the trips (adaptation region effect), or whether it is related to the formation mechanism of the boundary-layer cannot be assessed just by these results. However, note that the higher the Reynolds number the higher the modulation coefficient is expected; the trend followed in the outer part for the *Saw* case is a lower modulation coefficient yet a significantly higher (50%) Reynolds number. If one considers Fig. 14b any conclusion drawn about these results may be risky due to the influence of the proximity of the trips, on the other hand, it may be plausible that the counter-intuitive result for the trend of the Reynolds number implies that there is a fundamental modification of the eddy structure in the *Saw* case persistent further from the adaptation region.

5 Conclusion

The main differences between, on one hand, the high Reynolds number turbulent boundary-layers studied in the frame of artificially generated thick (atmospheric) boundary-layers and, on the other hand, high fidelity high Re experiments in the last decade or so is primarily due to the disparity between the distinct criteria applied to assess the validity of the results. Our study aimed at generating a high Reynolds number TBL that resembles the canonical properties to the highest accuracy. Results have shown that a boundary-layer of approximately 150% higher momentum thickness (or equivalently, Reynolds number) can be formed after an adaptation region using spanwise arrays of cylinders (with constant blockage in the wall-normal direction) for the same downstream distance ($x \approx 3$ m) compared with the *Natural* case. This result is highly relevant when studying high Reynolds number wall-bounded flows in short wind tunnels. On the other hand, obstacles with a non-uniform blockage in y with 100% blockage at the wall, do not generate canonical properties even after a long recovery distance. It has also been shown that the degree of immersion in the TBL ($h/\delta_\gamma \ll 1$ or $h/\delta_\gamma \approx 1$) is less significant than the formation mechanism.

Study of spectra and two-point velocity measurement showed that this is possibly due to different mechanisms of formations downstream of the trips. The cylinders do not destroy the inner structures of the flow, which then grow entraining the cylinder wakes (*wall driven*); this is in contrast to the sawtooth, which forms the inner behaviour at a certain length downstream of the trips with a higher influence of the outer eddies detached from the trips (*wake driven*). The question of whether the different behaviour of the sawtooth is due to the non-uniform blockage (and therefore the shear generated) or because the blockage is 100% for $y = 0$ remains unclear but the latter appears more reasonable. Detailed study of the formation mechanisms and the outer-inner interactions has been conducted by two-point measurements at different downstream locations in order to study eddy structure and modulation effects. The results appear to confirm the existence of two well-differentiated formation mechanisms. In particular, these results show that a non-canonical behaviour concerning modulation and eddy-structure is maintained in the *Saw* case up to the last downstream position measured presenting a clear scaling in outer variables. Thus it can be surmised that there are fundamental changes in the structure of the TBL that are probably due to two different formation mechanisms.

References

Adrian RJ (2007) Hairpin vortex organization in wall turbulence. Phys Fluids 19(4):041,301

Alving AE, Fernholz H (1996) Turbulence measurements around a mild separation bubble and downstream of reattachment. J Fluid Mech 322:297–328

Arie M, Kiya M, Suzuki Y, Sakata I (1981) Artificial Generation of Thick Turbulent Boundary Layers. The Japan Society of Mechanical Engineers 24(192):956–964

Armitt J, Counihan J (1968) The Simulation of the Atmospheric Boundary Layer in a Wind Tunnel. Atmos Environ 2(1):49–71

Bailey SCC, Kunkel GJ, Hultmark M, Vallikivi M, Hill JP, Meyer Ka, Tsay C, Arnold CB, Smits AJ (2010) Turbulence measurements using a nanoscale thermal anemometry probe. J Fluid Mech 663:160–179

Boppe RS, Neu WL, Shuai H (1999) Large-scale motions in the marine atmospheric surface layer. Boundary-Layer Meteorol 92(2):165–183

Brown GL, Thomas ASW (1977) Large structure in a turbulent boundary layer. Phys Fluids 20(10):243–252

Castro I, Epik E (1998) Boundary layer development after a separated region. J Fluid Mech 274:91–116

Chauhan KA, Monkewitz PA, Nagib HM (2009) Criteria for assessing experiments in zero pressure gradient boundary layers. Fluid Dyn Res 41(2):021,404

Chernyshenko SI, Marusic I, Mathis R (2012) Quasi-steady description of modulation effects in wall turbulence. arXiv:12033714v1 [physicsflu-dyn] p 16, 1203.3714

Comte-bellot G (1976) Hot-wire anemometry. Annu Rev of Fluid Mech 8:209–231

Cook N (1978) Wind-tunnel simulation of the adiabatic athmopheric boundary layer by roughness, barrier and mixing device methods. J industrial aerodynamics 3(2):157–176

Counihan J (1969) An improved method of simulating an atmospheric boundary layer in a wind tunnel. Atmos Environ 3(2):197–214

Davidson MJ, Snyder WH, Lawson RE, Hunt JCR (1996) Wind tunnel simulation of plume dispersion through groups of obstacles. Atmos Environ 30(22):3715–3731

DeGraaf DB, Eaton JK (2000) Reynolds-number scaling of the flat-plate turbulent boundary layer. J Fluid Mech 422:319–346

Favre A, Gaviglio J, Dumas R (1957) Space-time double correlations and spectra in a turbulent boundary layer. J Fluid Mech 2(4):313–342

Hunt JCR, Fernholz H (1975) Wind-tunnel simulation of the atmospheric boundary layer: a report on Euromech 50. J Fluid Mech 70(3):543

Hutchins N, Marusic I (2007a) Evidence of very long meandering features in the logarithmic region of turbulent boundary layers. J Fluid Mech 579:1–28

Hutchins N, Marusic I (2007b) Large-scale influences in near-wall turbulence. Philos trans R Soc A 365(1852):647–64

Hutchins N, Nickels TB, Marusic I, Chong MS (2009) Hot-wire spatial resolution issues in wall-bounded turbulence. J Fluid Mech 635:103–136

Klebanoff P (1954) Characteristics of Turbulence in a Boundary Layer with Zero Pressure Gradient. Tech. rep., National Advisory Comitee for Aeronautics Report 1247

Klewicki JC (2010) Reynolds Number Dependence, Scaling, and Dynamics of Turbulent Boundary Layers. J Fluids Eng 132(9):094,001

Kornilov VI, Boiko aV (2012) Wind-tunnel simulation of thick turbulent boundary layer. Thermophys and Aeromech 19(2):247–258

Kornilov VI, Boiko aV (2013) Simulation of a thick turbulent boundary layer via a rod grid. Thermophys and Aeromech 20(3):289–302

Marusic I, Heuer WDC (2007) Reynolds Number Invariance of the Structure Inclination Angle in Wall Turbulence. Phys Rev Lett 99(11):114,504

Marusic I, McKeon BJ, Monkewitz Pa, Nagib HM, Smits aJ, Sreenivasan KR (2010) Wall-bounded turbulent flows at high Reynolds numbers: Recent advances and key issues. Phys Fluids 22(6):065,103

Marusic I, Mathis R, Hutchins N (2011) A wall-shear stress predictive model. J Phys Conf Ser 318(1):012,003

Mathis R, Hutchins N, Marusic I (2009) Large-scale amplitude modulation of the small-scale structures in turbulent boundary layers. J Fluid Mech 628:311–337

Mathis R, Hutchins N, Marusic I (2011) A predictive inner-outer model for streamwise turbulence statistics in wall-bounded flows. J Fluid Mech 681:537–566

Mathis R, Marusic I, Chernyshenko SI, Hutchins N (2013) Estimating wall-shear-stress fluctuations given an outer region input. J Fluid Mech 715:163–180

Mazellier N, Vassilicos JC (2010) Turbulence without Richardson-Kolmogorov cascade. Phys Fluids 22(7):075,101, arXiv:0911.0841v2

McKeon BJ, Li J, Jiang W, Morrison JF, Smits aJ (2003) Pitot probe corrections in fully developed turbulent pipe flow. Meas Sci and Technol 14(8):1449–1458

Metzger MM, Klewicki JC (2001) A comparative study of near-wall turbulence in high and low Reynolds number boundary layers. Phys Fluids 13(3):692–701

Nagib HM, Morkovin MV, Yung JT, Tan-atichat J (1976) On Modeling of Atmospheric Surface Layers by the Counter-Jet Technique. AIAA Journal 14(2):185–190

Nagib HM, Chauhan Ka, Monkewitz Pa (2007) Approach to an asymptotic state for zero pressure gradient turbulent boundary layers. Philos trans R Soc A 365:755–770

Nickels TB, Marusic I, Hafez S, Hutchins N, Chong MS (2007) Some predictions of the attached eddy model for a high Reynolds number boundary layer. Philos trans R Soc A 365(1852):807–22

Österlund JM (1999) Experimental studies of zero pressure-gradient turbulent boundary layer flow Experimental Studies of Zero Pressure-Gradient Turbulent Boundary-Layer Flow. PhD thesis, Royal Institute of Technology, p 194

Phillips OM (1955) The irrotational motion outside a free turbulent boundary. Math Proc Cam Philol Soc 51(01):220

Robinson SK (1986) Instantaneous Velocity Profile Measurements in a Turbulent Boundary Layer. Chem Eng Commun 43(4):347–369

Rodríguez-López E, Bruce PJK, Buxton ORH (2015a) A robust post-processing method to determine skin friction in turbulent boundary layers from the velocity profile. Exp Fluids 56(4):68 1–16

Rodríguez-López E, Bruce PJK, Buxton ORH (2015b) Downstream evolution of perturbations in a zero pressure gradient turbulent boundary layer. In: Progress in turbulence VI, Proceedings of the iTi conference in Turbulence 2014. *(To appear)*, 21-24 September, Bertinoro, Italy

Sargison JE, Walker GJ, Bond V, Chevalier G (2004) Experimental review of devices to artificially thicken wind tunnel boundary layers. In: 15th Australasian Fluid Mechanics Conference, 13-17 December, Sidney, Australia

Simens MP, Jimenez J, Hoyas S, Mizuno Y (2009) A high-resolution code for turbulent boundary layers. J Comput Phys 228(11):4218–4231

Talamelli A, Persiani F, H M Fransson J, Alfredsson PH, V Johansson A, M Nagib H, Rüedi JD, R Sreenivasan K, A Monkewitz P (2009) CICLoPE-a response to the need for high Reynolds number experiments. Fluid Dyn Res 41(2):021,407

Taylor G (1938) The spectrum of turbulence. Philos trans R Soc A 164:476–490

Townsend A (1976) The Structure of Turbulent Shear Flow, 2nd edn. Cambridge university Press, Cambridge and New York, p 438

Valente PC, Vassilicos JC (2014) The non-equilibrium region of grid-generated decaying turbulence. J Fluid Mech 744:8–37

Vinuesa R (2013) Synergetic computational and experimental studies of Wall-bounded turbulent flows and their two-dimensionality. PhD thesis, Illinois Institute Technology. Chicago